



# Crystal structure and thermoelectric properties of $\text{Cu}_2\text{Cd}_{1-x}\text{Zn}_x\text{SnSe}_4$ solid solutions



F.S. Liu, B. Wang, W.Q. Ao, Y. Li, J.Q. Li\*

College of Materials Science and Engineering, Shenzhen University and Shenzhen Key Laboratory of Special Functional Materials, Shenzhen 518060, PR China

## ARTICLE INFO

### Article history:

Received 8 April 2014

Received in revised form

24 June 2014

Accepted 25 June 2014

Available online 21 July 2014

### Keywords:

A. Functional alloys

B. Thermoelectric properties

F. X-ray diffraction

## ABSTRACT

$\text{Cu}_2\text{Cd}_{1-x}\text{Zn}_x\text{SnSe}_4$  solid solutions were synthesized, and their phase constitutions and thermoelectric properties were investigated. The solid solutions crystallized in the stannite-type structure for Zn contents  $x$  up to 0.65 and in the kesterite-type structure for  $0.7 \leq x \leq 1.0$ . The lattice parameter  $a$  and cell volume  $V$  of the compounds decreased linearly with increasing  $x$  for both the stannite-type ( $0 \leq x \leq 0.65$ ) and the kesterite-type ( $0.7 \leq x \leq 1$ ) structures. The lattice parameter  $c$  decreased with increasing  $x$  for the compounds with the kesterite-type structure but increased for the compounds with the stannite-type structure. The  $c/a$  ratio increased with increasing Zn content, which indicated an weakening of the lattice distortion. The Seebeck coefficient tended to decrease with increasing Zn content, whereas the electrical conductivity and thermal conductivity increased. The figure of merit  $ZT$  increased with increasing  $x$  over the composition range of  $0 \leq x \leq 0.60$  and then fluctuated with a further increase in  $x$ . A maximum  $ZT$  of 0.23 was achieved for  $\text{Cu}_2\text{Cd}_{0.4}\text{Zn}_{0.6}\text{SnSe}_4$  at 720 K.

© 2014 Elsevier Ltd. All rights reserved.

## 1. Introduction

The thermoelectric effect is the direct conversion of a temperature difference into electrical voltage and vice-versa on the basis of the Seebeck effect or Peltier effect, respectively. Thermoelectric materials can be used as power generators, coolers, and thermal sensors [1,2]. The efficiency of a thermoelectric device depends on the dimensionless figure of merit  $ZT$ :  $ZT = S^2\sigma T/\kappa$  [3,4], where  $S$  is the Seebeck coefficient,  $\kappa$  is the thermal conductivity,  $\sigma$  is the electrical conductivity, and  $T$  is the absolute temperature. Thus, the thermoelectric performance of a material can be improved by enhancing its Seebeck coefficient and electrical conductivity and by reducing its thermal conductivity [5].

High-performance thermoelectric materials that operate in intermediate-temperature ranges often contain lead (Pb), especially p-type thermoelectric materials such as  $\text{PbTe-SrTe}$  [6] ( $ZT = 2.2$  at 915 K) and  $\text{AgPb}_m\text{SbTe}_{2+m}$  (LAST-m) ( $ZT = 2.2$  at 800 K) [7]. It is well-known that the presence of lead in the environment causes toxic effects in plants and animals. Therefore, exploring novel thermoelectric materials with high  $ZT$ s that are lead free and that

are composed of elements that are abundant in the Earth's crust remains an interesting topic for researchers.

Cu-based intermetallics or minerals have been found to possess promising thermoelectric properties [8–10]. The quaternary compounds  $\text{Cu}_2\text{ZnSnSe}_4$  and  $\text{Cu}_2\text{CdSnSe}_4$  have aroused considerable research interest from scientists in recent years [11]. These materials have notable thermoelectric properties, such as stabilized p-type conductivity, a relatively high Seebeck coefficient, and a relatively low lattice thermal conductivity. The compounds  $\text{Cu}_2\text{ZnSnSe}_4$  and  $\text{Cu}_2\text{CdSnSe}_4$  are potential intermediate-temperature thermoelectric materials. The  $ZT$  values reach 0.9 at 860 K for  $\text{Cu}_{2.1}\text{Zn}_{0.9}\text{SnSe}_4$  [12], 0.95 at 850 K for  $\text{Cu}_2\text{ZnSn}_{0.9}\text{In}_{0.1}\text{Se}_4$  [13], 0.3 at 720 K for  $\text{Cu}_{2.05}\text{ZnSn}_{0.95}\text{Se}_4$  [14], and 0.65 at 723 K for colloidal-synthesized  $\text{Cu}_2\text{CdSnSe}_4$  [15].

Both the  $\text{Cu}_2\text{ZnSnSe}_4$  and  $\text{Cu}_2\text{CdSnSe}_4$  quaternary compounds possess body-centered tetragonal symmetry. The Cu, Cd, Zn, and Sn atoms are all coordinated with Se atoms in a tetrahedral manner. The oxidation states of Cu, Cd, Zn, Sn, and Se in the structure are +1, +2, +2, +4, and −2, respectively [16]. The compound  $\text{Cu}_2\text{ZnSnSe}_4$  crystallizes in the kesterite-type crystal structure with the space group  $\bar{I}4$  as confirmed by powder X-ray diffraction (XRD) and neutron scattering [17] measurements, whereas  $\text{Cu}_2\text{CdSnSe}_4$  crystallizes in the stannite-type structure belonging to space group  $\bar{I}42m$  [18]. The differences in atomic sites between these two compounds can be described as follows. When all of the Sn atoms

\* Corresponding author. Tel./fax: +86 75526536239.

E-mail address: [junqinli@szu.edu.cn](mailto:junqinli@szu.edu.cn) (J.Q. Li).

exchange sites with half of the Cu atoms in the  $\text{Cu}_2\text{CdSnSe}_4$   $I\bar{4}2m$  cell, the structure transforms from the stannite-type to the kesterite-type.  $\text{Cu}_2\text{CdSnSe}_4$  can be divided into two structural/functional units: a  $\text{Cu}_2\text{Se}_4$  tetrahedral array that acts as an electrically conducting unit and a  $\text{CdSnSe}_4$  tetrahedral array that acts as an insulating unit, satisfying the requirements for being classified as a Slack's phonon glass electron crystal (PGEC) [19]. PGEC materials exhibit high electrical conductivity, similar to a crystal, but low thermal conductivity, similar to a glass. The electrically insulating  $\text{CdSnSe}_4$  unit responsible for the low thermal conductivity is inserted between two electrically conducting  $\text{Cu}_2\text{Se}_4$  units, which account for the electrical conductivity [12]. Recently, considerable interest has arisen in the study of the thermoelectric properties of wide-band-gap quaternary compounds because conventional thermoelectric materials exhibit a narrow band gap, where a bipolar effect may reduce the thermoelectric efficiency [14]. The reported band gap  $E_g$  is 1.44 eV for  $\text{Cu}_2\text{ZnSnSe}_4$  and 0.96 eV for  $\text{Cu}_2\text{CdSnSe}_4$  [20].

With respect to the thermoelectric properties of the compounds  $\text{Cu}_2\text{ZnSnSe}_4$  and  $\text{Cu}_2\text{CdSnSe}_4$ ,  $\text{Cu}_2\text{ZnSnSe}_4$  exhibits lower resistivity, whereas  $\text{Cu}_2\text{CdSnSe}_4$  manifests lower thermal conductivity. The structural transition and thermoelectric properties of the alloys in the  $\text{Cu}_2\text{ZnSnSe}_4$ – $\text{Cu}_2\text{CdSnSe}_4$  pseudo-binary system have not yet been reported. In terms of element doping or composite materials,  $\text{Cu}_2\text{Cd}_x\text{Zn}_{1-x}\text{SnSe}_4$  solid solutions or alloys in the two-phase region may exhibit good thermoelectric properties combined with the advantages of both the end compounds. In this work, we prepared a series of  $\text{Cu}_2\text{Cd}_x\text{Zn}_{1-x}\text{SnSe}_4$  samples with  $x = 0$  to 1 using melt-quenching and spark plasma sintering (SPS). The crystal structure and thermoelectric performance of the samples were investigated in detail.

## 2. Experimental details

High purity Cu (99.99%), Zn (99.99%), Cd (99.99%), Sn (99.99%), and Se (99.99%) were used as the starting materials; they were weighed in the desired ratios and sealed in quartz tubes under vacuum ( $<10^{-2}$  Pa). The tubes were placed in a furnace and slowly heated to 1273 K at a heating rate of 1 K  $\text{min}^{-1}$ . The alloys were held at 1273 K for 24 h were subsequently cooled slowly to 773 K and maintained at this temperature for 120 h before being quenched in liquid nitrogen. The quenched alloys were powdered in an agate mortar and then ball-milled in a planetary ball mill (QM-4F, Nanjing University, China) at 200 rpm for 12 h using a hard stainless steel vial and zirconia balls. The weight ratio of balls to powder was maintained at approximately 6:1, and the mill vial was evacuated and then filled with a pure  $\text{H}_2$  atmosphere to prevent the powder from oxidizing during the milling process. The powders were pressed into pellet form and annealed at 773 K for 200 h in sealed, evacuated quartz tubes. The pellets were then ground into a fine powder and consolidated by SPS at 923 K for 5 min under a vacuum of  $10^{-2}$  Pa or better and a pressure of 48 MPa in a graphite die with a peak current impulse value of 703 A. The density of the bulk sample obtained after SPS was greater than 97% of the theoretical value. Bar specimens with typical dimensions of 13.0 mm  $\times$  4.0 mm  $\times$  4.0 mm were prepared for electrical property measurements, and disk specimens with a diameter of 10.0 mm and a thickness of 2.0 mm were prepared for thermal conductivity measurements.

The phases in the samples were analyzed by X-ray diffraction (XRD) on a Bruker D8 Advance SS/18 kW diffractometer equipped with a Cu  $K\alpha$  radiation source; the samples were scanned in the  $2\theta$  range between 10 and 120°. Rietveld refinement of the XRD patterns was performed using the software Topas 3.1 [21]. The Seebeck coefficient  $S$  and the electric conductivity  $\sigma$  were measured on a ZEM-2 (Ulvac-Riko, Japan) under a helium atmosphere; the measurement errors were approximately 7% and 10%, respectively. The

thermal diffusivity ( $\alpha$ ) and the specific heat capacity  $C_p$  were measured simultaneously via a laser flash method on a TC-9000h thermal constants measuring system under a vacuum of  $1.0 \times 10^{-3}$  Pa. The bulk density  $\rho_m$  of the sample was calculated from the sample's geometry and mass. The thermal conductivity  $\kappa$  of the samples was calculated according to the equation  $\kappa = \alpha C_p \rho_m$ ; the estimated error of the measurements was approximately 13%. DSC experiments were performed on a SETARAM 16–18 Evolution using a constant heat rate of 5 K  $\text{min}^{-1}$ .

## 3. Results and discussion

### 3.1. Crystal structure

The XRD patterns of the SPS-sintered  $\text{Cu}_2\text{Cd}_{1-x}\text{Zn}_x\text{SnSe}_4$  ( $x = 0$ –1.0) samples are presented in Fig. 1. These patterns can be identified as resulting from the compound with the space group  $I\bar{4}2m$  or  $I\bar{4}$  in the tetragonal system, without any contribution of a second phase (Fig. 1(a)). The intensities of the strongest peak (112) of the patterns were normalized to evaluate the intensity of the other peaks as a function of the zinc content  $x$ . Fig. 1(a) reveals that most of the peaks shifted to higher angles with increasing zinc content  $x$ . The (220) and (024) peaks at a  $2\theta$  angle of approximately 45.0° and the (116) and (132) peaks at a  $2\theta$  angle of approximately 52.5° split in the pattern of the sample with  $x = 0$  but overlapped gradually as  $x$  was increased to 1.0. With increasing zinc content  $x$ , the intensities of the (002), (110), (022), and (114) peaks decreased; however, those of the (011), (013), (121), and (123) peaks increased substantially (Fig. 1(b)).

We cannot distinguish between two symmetries of  $I\bar{4}$  and  $I\bar{4}2m$  on the basis of the XRD results because the extinction conditions for these two space groups are identical. However, we can identify them by Rietveld refinement on the basis of the reliability factors  $R_{wp}$  and  $R_{Bragg}$ , which are calculated from the intensity using the symmetry and atomic occupations.  $R_{wp}$  reveals the goodness of the whole profile fit, and  $R_{Bragg}$  provides a valuable indication of the suitability of the structural model. In the refinement process, Zn and Cd atoms are fixed to occupy the same site; however, their occupancies are free for refining. Both the stannite- and the kesterite-type structure models were used to refine each XRD pattern. As illustrated in Fig. 1(a), the patterns were divided into two groups: group A for the samples with  $x = 0, 0.1, 0.2, 0.3, 0.5, 0.55, 0.6$ , or  $0.65$  and group B for the samples with  $x = 0.7, 0.8, 0.9$ , or  $1.0$ . When the stannite-type structure model for the samples in group A or the kesterite-type structure model for the samples in group B was used, the  $R_{wp}$  was approximately 3%, the  $R_{Bragg}$  was 0.35–1% (Table 1), and the occupancies of the Zn and Cd atoms were close to the nominal composition. In contrast, when the kesterite-type structure model was used for the samples in group A or the stannite-type structure model for the samples in group B, the  $R_{wp}$  increased to more than 5%, the  $R_{Bragg}$  increased to more than 30%, and the occupancies of the Zn and Cd atoms exhibited obvious deviations from the nominal composition. Because of the strong diffraction intensity collected by the LynxEye array detector, the goodness of fit factor ( $R_{wp}/R_{exp}$ ) was approximately 2–3, which is slightly larger than 2. However, the low values of  $R_{wp}$  and  $R_{Bragg}$  and the consistency of the occupancies of the Zn and Cd atoms confirmed the reliability of the results obtained by Rietveld refinement. The results confirmed that the samples in group A belong to the stannite-type structure with space group  $I\bar{4}2m$ , whereas the samples in group B are of the kesterite-type structure with space group  $I\bar{4}$  (Fig. 1(a)).

The FWHM of the (112) peak with the maximum intensity obtained by fitting of the peak profile shows that there is no obvious broadening of the (112) peak of the samples with different  $x$  values

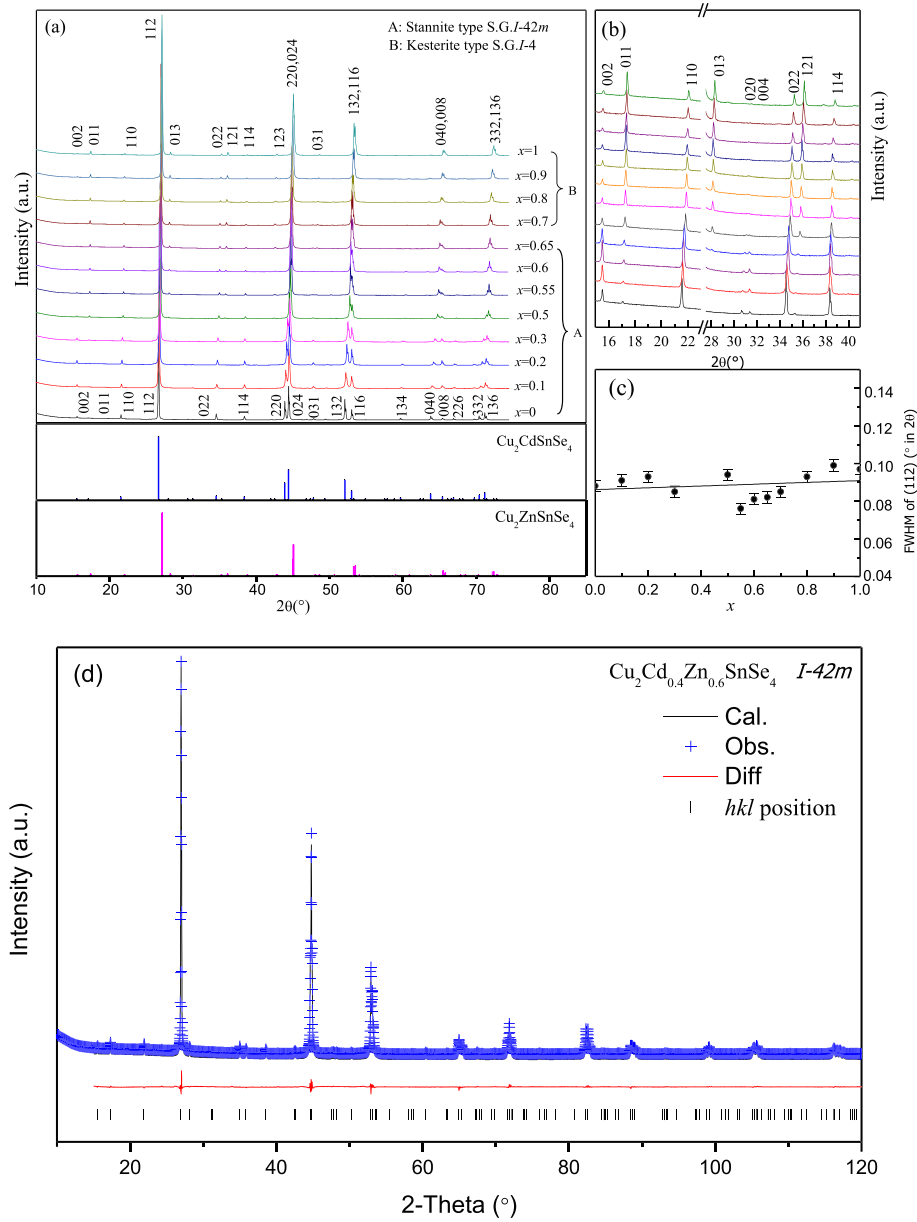


**Fig. 1.** (a) Powder XRD patterns of  $\text{Cu}_2\text{Cd}_{1-x}\text{Zn}_x\text{SnSe}_4$ ; (b) partial details of the XRD patterns (the stacking order is the same as that in (a)); (c) FWHM of the (112) peaks; (d) XRD Rietveld refinement results for the  $x = 0.6$  alloy.

**Table 1**

Lattice parameters ( $a$ ,  $c$ , and  $V$ ),  $c/a$  ratio, mean atomic weight ( $M$ ), calculated density ( $\rho_c$ , g/cm<sup>3</sup>), melting point ( $T_m$ ), value of  $(T_m^{3/2} \rho^{2/3})/M^{7/6}$  ( $\kappa_0$ , K<sup>3/2</sup>g<sup>2/3</sup>cm<sup>-2</sup>), and reliability factors ( $R_{\text{exp}}$ ,  $R_{\text{wp}}$ , and  $R_{\text{Bragg}}$ , %) for the Rietveld refinements of  $\text{Cu}_2\text{Cd}_{1-x}\text{Zn}_x\text{SnSe}_4$ .

$x$	$a(\text{\AA})$	$c(\text{\AA})$	$V(\text{\AA}^3)$	$c/a$	$M$	$\rho_c$	$R_{\text{exp}}$	$R_{\text{wp}}$	$R_{\text{Bragg}}$	$T_m(\text{K})$	$\kappa_0$
0	5.829(1)	11.403(1)	387.5(1)	1.956	84.25	5.776	0.94	2.40	1.01	1040	612.04
0.1	5.813(1)	11.409(1)	385.5(1)	1.962	83.67	5.764	0.85	2.27	0.61	1044	619.76
0.2	5.797(1)	11.415(1)	383.6(1)	1.969	83.08	5.753	0.83	2.44	0.60	1047	626.78
0.3	5.782(1)	11.418(1)	381.7(1)	1.975	82.49	5.741	0.83	2.36	0.35	1048	632.02
0.5	5.756(1)	11.421(1)	378.5(1)	1.984	81.31	5.718	0.84	2.38	0.41	1053	645.57
0.55	5.745(1)	11.422(1)	377.0(1)	1.988	81.02	5.616	0.82	2.93	0.58	1050	637.83
0.6	5.740(1)	11.419(1)	376.2(1)	1.989	80.73	5.604	0.81	2.78	0.75	1052	641.46
0.65	5.732(1)	11.414(1)	375.1(1)	1.991	80.43	5.587	0.80	2.82	0.68	1046	637.40
0.7	5.727(1)	11.410(1)	374.2(1)	1.992	80.14	5.686	0.82	2.89	1.00	1045	646.74
0.8	5.714(1)	11.392(1)	372.0(1)	1.993	79.55	5.676	0.84	2.29	0.53	1049	655.30
0.9	5.703(1)	11.370(1)	369.8(1)	1.994	78.96	5.666	0.83	2.33	0.55	1057	667.78
1	5.693(1)	11.345(1)	367.7(1)	1.993	78.38	5.657	0.82	2.99	0.64	1061	676.74

(Fig. 1(c)). This result indicates that all of the samples are a single stannite- or kesterite-type phase. The two-phase region between the stannite- and the kesterite-type solid solutions appears narrow, between  $x = 0.65$  and  $x = 0.70$ . Notably, however, slight atomic disorder may exist in the samples with  $x = 0.55, 0.60, 0.65$ , or  $0.70$  because of the relatively higher  $R_{wp}$  or  $R_{Bragg}$ . When the site disorder was refined for the Cu and Sn atoms, approximately 12% of the Sn atoms exchanged sites with Cu atoms in the sample with  $x = 0.7$ , and the  $R_{Bragg}$  factor decreased from 1% to 0.76%. Because the atomic scattering factors of Cu and Zn are similar, as are those of Sn and Cd, the degree of disorder cannot be determined from the XRD Rietveld refinement. As previously described, the main structural difference between the stannite-type  $\text{Cu}_2\text{CdSnSe}_4$  and the kesterite-type  $\text{Cu}_2\text{ZnSnSe}_4$  is the exchange of Sn atoms with half of the Cu atoms. Therefore, the structural transformation between the stannite-type and kesterite-type may be accomplished using atomic disorder in  $\text{Cu}_2\text{Cd}_{1-x}\text{Zn}_x\text{SnSe}_4$  alloys.

The lattice parameters and reliability factors for the compounds obtained by Rietveld refinement are listed in Table 1, and the refined atomic parameters for  $\text{Cu}_2\text{CdSnSe}_4$  and  $\text{Cu}_2\text{ZnSnSe}_4$  are listed in Table 2. A representative XRD Rietveld refined pattern for the sample with  $x = 0.6$  is presented in Fig. 1(d). The lattice parameters are plotted as a function of the zinc content  $x$  in Fig. 2. It is observed that the lattice parameter  $a$  and cell volume ( $V$ ) decrease linearly with increasing Zn content  $x$  for the compounds in both groups, but with different slopes. This result illustrates the substitution of larger  $\text{Cd}^{2+}$  ions (0.78 Å) by smaller  $\text{Zn}^{2+}$  ions (0.60 Å) in the structure [22]. The lattice parameter  $c$  increases linearly for the stannite-type compounds but decreases for the kesterite-type compounds with increasing  $x$ . This finding may account for the bonding anisotropy in the  $ab$  plane and along the  $c$  direction. The linear relationships between the lattice parameters and zinc content  $x$  can be expressed as follows:  $a_s(\text{Å}) = 5.828(1) - 0.149(3)x$ ;  $c_s(\text{Å}) = 11.408(3) + 0.0177(9)x$  and  $V_s(\text{Å}^3) = 387.549(4) - 19.098(1)x$  for stannite-type compounds, and  $a_k(\text{Å}) = 5.805(4) - 0.113(4)x$ ;  $c_k(\text{Å}) = 11.564(8) - 0.217(9)x$  and  $V_k(\text{Å}^3) = 389.4(2) - 21.7(3)x$  for kesterite-type compounds. The lattice parameter  $a$  also exhibits a linear relationship with the mean atomic weight ( $M$ ) of the compound as  $a_s(\text{Å}) = 0.025(1)M + 3.73(6)$ ;  $a_k(\text{Å}) = 0.019(1)M + 4.18(6)$ , which is similar to the formula reported by Matsushita et al. [20], where the subscript S refers to the stannite-type structure and K refers to the kesterite-type structure. If we view the structure of  $\text{Cu}_2\text{CdSnSe}_4$  as being derived from the cubic zinc blende structure, the lattice distortion can be estimated from the  $c/a$  ratio. When the zinc content  $x$  increases from 0 to 1.0, the  $c/a$  ratio gradually approaches 2 (Table 1), which means that a larger incorporation of Zn atoms leads to less lattice distortion.

The atomic distances between Se and M ( $M = \text{Cu, Zn/Cd, or Sn}$ ) are plotted as a function of the zinc content  $x$  in Fig. 3. All the Se–M bond lengths decrease with increasing  $x$  in both the stannite- and

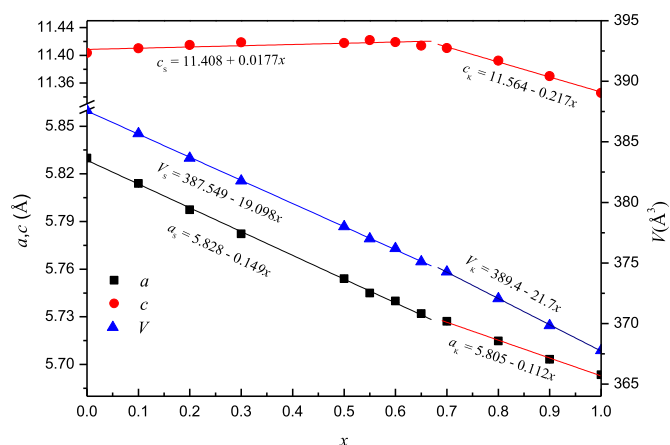


Fig. 2. Lattice parameters of  $\text{Cu}_2\text{Cd}_{1-x}\text{Zn}_x\text{SnSe}_4$  as a function of  $x$ . The formulas show the relationship between the lattice parameter and the zinc content  $x$ , where the subscript S refers to the stannite-type structure and K refers to the kesterite-type structure.

the kesterite-type samples. The kesterite-type samples have shorter Se–Sn bonds and longer Se–Cu bonds than those of the stannite-type samples.

The DSC curves for  $\text{Cu}_2\text{Cd}_x\text{Zn}_{1-x}\text{SnSe}_4$  presented in Fig. 4 reveals that the melting point ( $T_m$ ) increases with increasing zinc content  $x$  for both the stannite- and the kesterite-type compounds. The slight deviation for the samples with  $x = 0.55, 0.60$ , and  $0.65$  may be due to the existence of atomic disorder in the structure of these samples. The melting points for  $\text{Cu}_2\text{CdSnSe}_4$  and  $\text{Cu}_2\text{ZnSnSe}_4$  are 1040 K and 1061 K, respectively, which agrees with the values reported by Matsushita et al. [20]. The melting point of  $\text{Cu}_2\text{II-IV-VI}_4$  compounds has been determined to decrease linearly with increasing mean atomic weight ( $M$ ) as follows:  $T_m(^{\circ}\text{C}) = -8.72M + 1500$ . Our results indicate the following relationships:  $T_{ms}(^{\circ}\text{C}) = -4.2(4)M + 850(5)$  and  $T_{mk}(^{\circ}\text{C}) = -9.5(9)M + 1263(5)$ , where the subscript S refers to the stannite-type structure and K refers to the kesterite-type structure.

### 3.2. Thermoelectric properties

The temperature dependencies of the electrical transport properties for  $\text{Cu}_2\text{Cd}_{1-x}\text{Zn}_x\text{SnSe}_4$  are shown in Fig. 5. The electrical conductivity increases for the samples with  $x = 0$  to  $0.3$  with increasing temperature but decreases slightly for the others

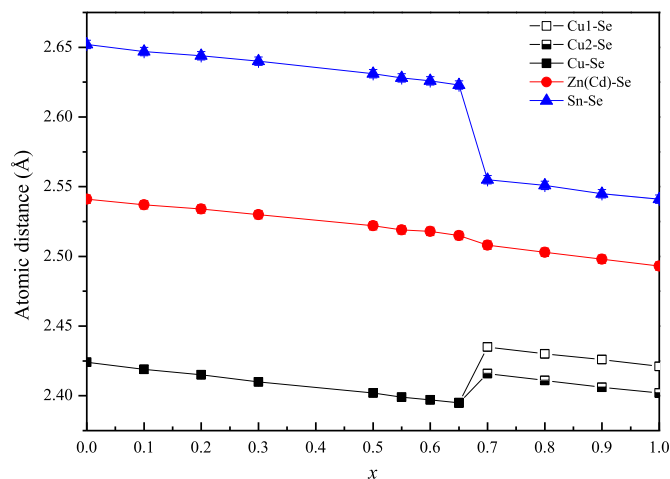


Fig. 3. Atomic distance of  $\text{Cu}_2\text{Cd}_{1-x}\text{Zn}_x\text{SnSe}_4$  as a function of  $x$ .

Table 2  
Atomic parameters for the  $\text{Cu}_2\text{CdSnSe}_4$  and  $\text{Cu}_2\text{ZnSnSe}_4$  compounds.

Atom	Site	$x$	$y$	$z$	Occupancy	$B$
<b><math>\text{Cu}_2\text{CdSnSe}_4</math></b>						
Cu	4d	0	0.5	0.25	1	0.9(1)
Cd	2a	0	0	0	1	0.2(1)
Sn	2b	0	0	0.5	1	0.7(2)
Se	8i	0.2585(1)	0.2585(1)	0.3617(1)	1	0.6(1)
<b><math>\text{Cu}_2\text{ZnSnSe}_4</math></b>						
Cu <sub>1</sub>	2a	0	0	0	1	0.2(1)
Cu <sub>2</sub>	2c	0	0.5	0.25	1	0.2(1)
Zn	2d	0.5	0	0.25	1	0.7(1)
Sn	2b	0.5	0.5	0	1	0.9(1)
Se	8g	0.2339(1)	0.2477(1)	0.1276(1)	1	0.9(1)

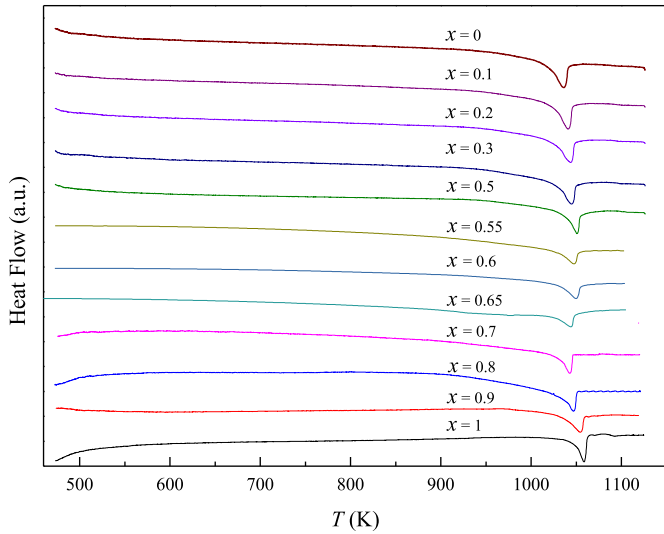


Fig. 4. DSC curves for  $\text{Cu}_2\text{Cd}_{1-x}\text{Zn}_x\text{SnSe}_4$ .

(Fig. 5(a)). The electrical conductivity also increases with the increasing Zn content  $x$ , except for fluctuations in the cases of the samples with  $0.55 \leq x \leq 0.70$  (Fig. 5(a), inset). The electrical conductivity for  $\text{Cu}_2\text{ZnSnSe}_4$  in this work was  $1.53 \times 10^4 \text{ S m}^{-1}$  at 300 K and  $0.78 \times 10^4 \text{ S m}^{-1}$  at 720 K, which are much higher than the values reported by Liu et al. [12] but lower than those reported by Shi et al. [13]. The electrical conductivity for the  $\text{Cu}_2\text{CdSnSe}_4$  in this work was  $1.6 \times 10^2 \text{ S m}^{-1}$  at 300 K and  $9.1 \times 10^2 \text{ S m}^{-1}$  at 720 K, which are slightly lower than the values reported by Liu et al. [12] and those of the samples prepared by nano-powder and chemical methods [15]. The differences in the reported electrical transport properties may be due to slight differences in the chemical composition, micro-structure, or trace second phase that result from the different synthesis methods. The electrical conductivities of these Cu-based quaternary compounds have been calculated as being generated from the hybridization of Cu 3d and Se 4p orbitals near the valence-band maximum (VBM) [16]. The Zn atoms doped into the  $\text{Cu}_2\text{CdSnSe}_4$  structure decrease the Cu–Se atomic distance, which may increase the concentration of carriers. However, the  $\text{Cu}_2\text{Se}_4$  tetrahedral array is a layer in the plane parallel to the  $ab$  plane in the structure of  $\text{Cu}_2\text{CdSnSe}_4$  separated by insulating  $\text{CdSnSe}_2$  tetrahedral slabs. In contrast, the distribution is reticular in the  $\text{Cu}_2\text{ZnSnSe}_4$  structure. Disorder of Cu and Zn atoms in the kesterite-type structure has also been observed [23,24], which may be due to the close cationic radii of  $\text{Cu}^+$  and  $\text{Zn}^{2+}$ . When the Zn atoms are doped into the structure of  $\text{Cu}_2\text{CdSnSe}_4$ , the Cu and Zn ions may also be disordered, which would provide more conduction channels, thereby resulting in greater electrical conductivity. Lattice distortion affects the banding length and thus the distribution of electrons near the Fermi surface, which may be another reason for the relationship between the electrical conductivity and the zinc content  $x$ .

The Seebeck coefficients and power factors increase with increasing temperature for all of the samples (Fig. 5(b and c)). The positive value of the Seebeck coefficient indicates  $P$ -type conduction for all the samples. Associated with the higher electrical conductivity for the samples with  $x = 0.55, 0.60$ , or  $0.65$ , the Seebeck coefficients for these samples are relatively lower (Fig. 5(b), inset). Except for these samples, the Seebeck coefficients for the other samples decrease with increasing Zn content  $x$ . The Seebeck coefficients, i.e.,  $109 \mu\text{V K}^{-1}$  at 300 K and  $219 \mu\text{V K}^{-1}$  at 720 K for  $\text{Cu}_2\text{ZnSnSe}_4$  and  $262 \mu\text{V K}^{-1}$  at 300 K and  $349 \mu\text{V K}^{-1}$  at 720 K for  $\text{Cu}_2\text{CdSnSe}_4$ , are higher than those of some well-known thermoelectric materials. The relationship between resistivity and the

Seebeck coefficient agrees with the traditional relationship between the concentration and mobility of the carrier. The power factor ( $P$ ) also increases with the Zn content  $x$ , except for fluctuations in the cases of the samples with  $0.55 \leq x \leq 0.70$  (Fig. 5(c)).

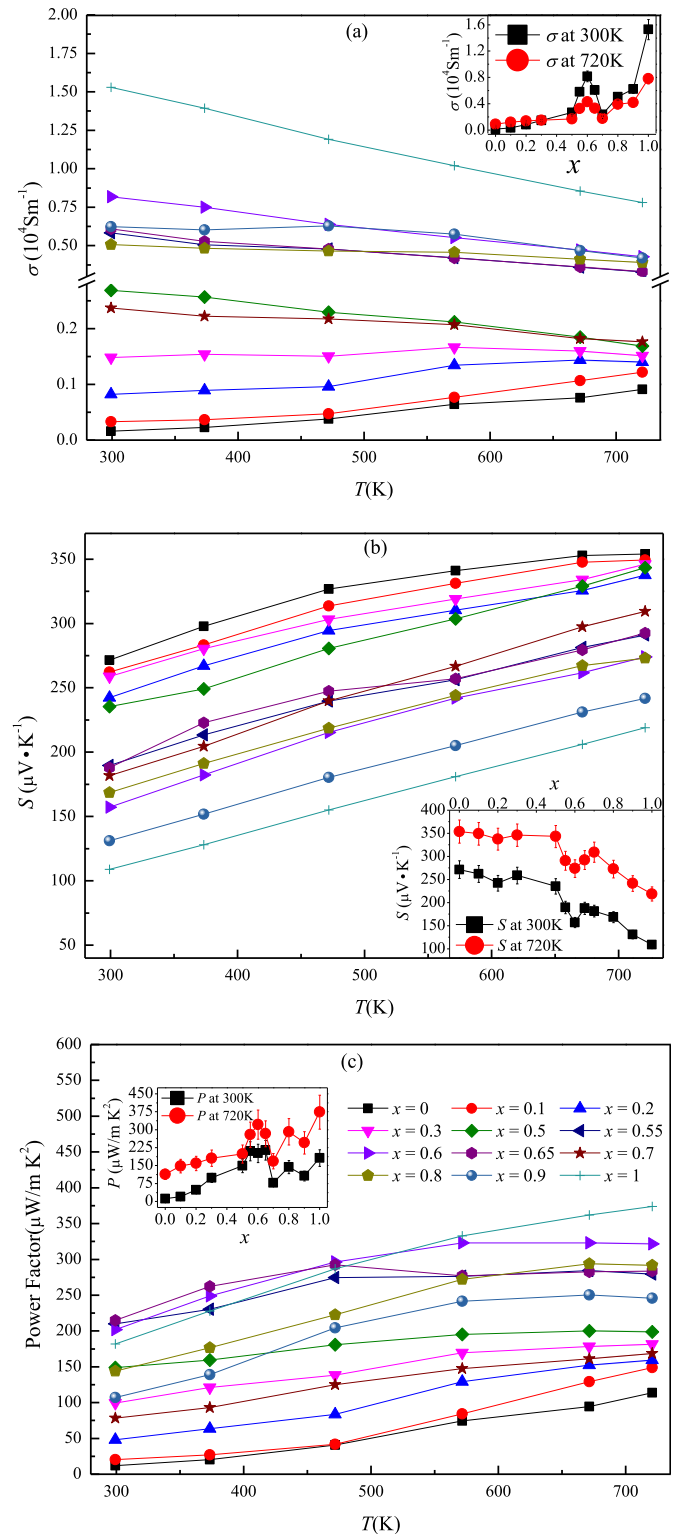
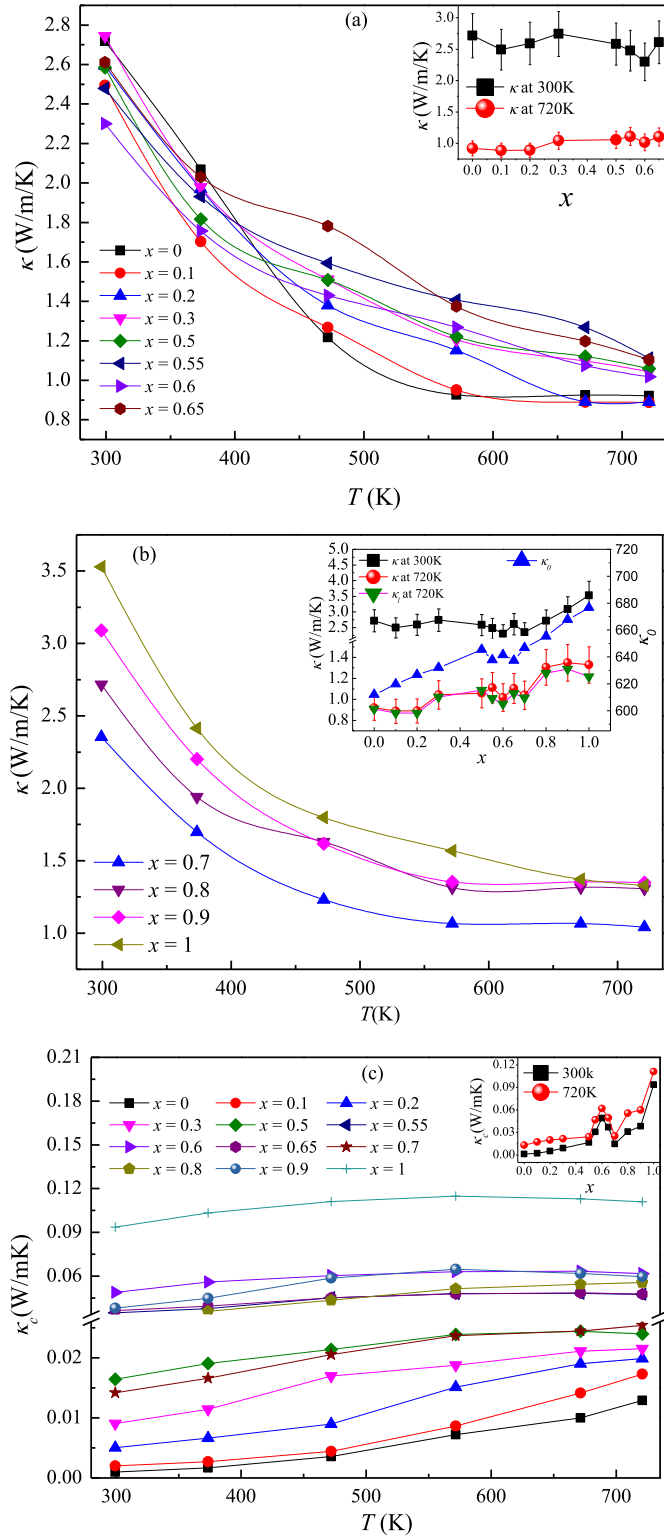


Fig. 5. Temperature dependence of the electrical conductivity (a); the Seebeck coefficient (b); and the power factor (c). The insets show the electrical conductivity, the Seebeck coefficient, and the power factor as functions of the Zn content  $x$  at 300 K and 720 K. The legends for (a) and (b) are the same as those for (c).





**Fig. 6.** The temperature dependence of the thermal conductivity of  $\text{Cu}_2\text{Cd}_{1-x}\text{Zn}_x\text{SnSe}_4$ : (a) total thermal conductivity ( $\kappa$ ) for  $x = 0, 0.1, 0.2, 0.3, 0.5, 0.55, 0.6$ , and  $0.65$ ; (b) total thermal conductivity ( $\kappa$ ) for  $x = 0.7, 0.8, 0.9$ , and  $1$ . The insets show the dependence of  $\kappa$  on the zinc content  $x$  at  $300\text{ K}$  and  $720\text{ K}$ , the lattice thermal conductivity ( $\kappa_l$ ), and the calculated value of  $Tm^{3/2}\rho_m^{2/3}/M^{7/6}(\kappa_0)$ ; (c) the calculated carrier thermal conductivity ( $\kappa_c$ ). The inset shows the dependence of  $\kappa_c$  on the zinc content  $x$  at  $300\text{ K}$  and  $720\text{ K}$ .

The temperature dependence of the thermal conductivity of  $\text{Cu}_2\text{Cd}_{1-x}\text{Zn}_x\text{SnSe}_4$  is demonstrated in Fig. 6(a and b). The compounds with the stannite-type structure exhibit lower thermal conductivity (Fig. 6(a)) compared with the compounds with the kesterite-type structure ( $x = 0.7, 0.8, 0.9, 1.0$ ) at both  $300\text{ K}$  and  $720\text{ K}$  (Fig. 6(b), inset). The lattice thermal conductivity ( $\kappa_l$ ) was calculated by subtracting the carrier thermal conductivity ( $\kappa_c$ ) from the total thermal conductivity ( $\kappa$ ). The carrier thermal conductivity  $\kappa_c$  was estimated using the Wiedemann–Franz relation  $\kappa_c = L_z\sigma T$ , where a Lorenz constant of  $L_z = 2.0 \times 10^{-8}\text{ W } \Omega \text{ K}^{-2}$  was applied for the estimation. The results indicate that  $\kappa_c$  is very small for all of the samples, with a maximum value of  $0.11\text{ W m}^{-1} \text{ K}^{-1}$  in  $\text{Cu}_2\text{ZnSnSe}_4$  at  $720\text{ K}$  (Fig. 6(c)) and therefore does not greatly affect the total thermal conductivity. The variation of the lattice thermal conductivity with the Zn content  $x$  exhibits the same tendency as the total thermal conductivity (Fig. 6(b), inset). This result indicates that the thermal conductivity is mainly dominated by the lattice conductivity. Therefore, the lower thermal conductivity of  $\text{Cu}_2\text{CdSnSe}_4$  is attributed to its greater lattice distortion compared to that in  $\text{Cu}_2\text{ZnSnSe}_4$ , which enhances phonon scattering by the lattice.

According to the Keyes expression [25], when the temperature is greater than the Debye temperature, the lattice thermal conductivity ( $\kappa_l$ ) is dominated primarily by phonon–phonon scattering:

$$\kappa_l T = \frac{R^{3/2}}{3\gamma^2 \epsilon^3 N_0^{1/3}} \frac{Tm^{3/2}\rho^{2/3}}{M^{7/6}} = B \frac{Tm^{3/2}\rho_m^{2/3}}{M^{7/6}},$$

where  $T_m$  is the melting point,  $M$  is the mean atomic weight,  $\gamma$  is the Grüneisen constant,  $\epsilon$  is the amplitude of interatomic thermal vibration,  $R$  is the ideal gas constant,  $N_0$  is Avogadro's number, and  $\rho$  is the density. Keyes stated that  $B$  can be regarded as a constant to estimate the lattice thermal conductivity at high temperatures. On the basis of the data listed in Table 1, the calculated value of  $\kappa_0 = Tm^{3/2}\rho_m^{2/3}/M^{7/6}$  increases with increasing Zn content  $x$ , which agrees with the relationship between thermal conductivity and the zinc content  $x$  at  $720\text{ K}$  (Table 1 and Fig. 6(b), inset).

The  $ZT$  calculated from the data above, as shown in Fig. 7, increases sharply with increasing temperature because the power factor increases while the thermal conductivity decreases. The  $ZT$  for  $\text{Cu}_2\text{Cd}_{1-x}\text{Zn}_x\text{SnSe}_4$  increases with increasing Zn content  $x$  up to  $x = 0.60$  and then fluctuates with a further increase in  $x$ . Because of its relatively higher electrical conductivity and lower thermal

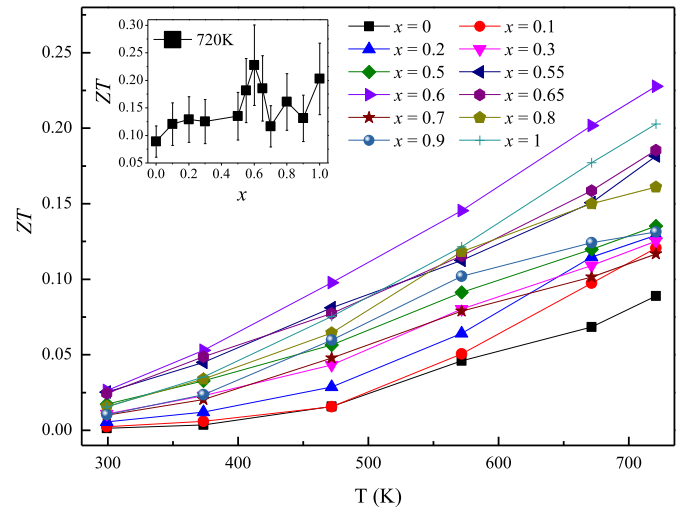


**Fig. 7.** Temperature dependence of the dimensionless figure of merit ( $ZT$ ) of  $\text{Cu}_2\text{Cd}_{1-x}\text{Zn}_x\text{SnSe}_4$ . The insets show  $ZT$  as a function of the Zn content  $x$  at  $720\text{ K}$ .

conductivity,  $\text{Cu}_2\text{Cd}_{0.4}\text{Zn}_{0.6}\text{SnSe}_4$  has a maximum  $ZT$  value of 0.23 at 720 K (Fig. 6, inset). The  $ZT$  values of the solid solutions in this system primarily depend on the electrical conductivity. The electrical conductivity increased from  $910 \text{ S m}^{-1}$  to  $7812 \text{ S m}^{-1}$ , whereas the power factor increased more than three-fold as the zinc content  $x$  increased from 0 to 1 at 720 K. However, the thermal conductivity only increased from  $0.91 \text{ W m}^{-1} \text{ K}^{-1}$  to  $1.32 \text{ W m}^{-1} \text{ K}^{-1}$  at the same temperature. This result may imply that the low electrical conductivity leads to a low  $ZT$  value in the solid solution. The electrical conductivity of  $\text{Cu}_{2.1}\text{Zn}_{0.9}\text{SnSe}_4$  reached  $33,200 \text{ S m}^{-1}$  by Cu-doping, and the  $ZT$  value reached 0.9 at 860 K [12]. Therefore, increasing the carrier concentration is one of the most effective routes to further enhance the thermoelectric performances of the  $\text{Cu}_2\text{CdSnSe}_4$  and  $\text{Cu}_2\text{ZnSnSe}_4$  solid solutions.

#### 4. Conclusions

In  $\text{Cu}_2\text{Cd}_{1-x}\text{Zn}_x\text{SnSe}_4$  solid solutions, the lattice parameters for both the stannite-type ( $x = 0, 0.1, 0.2, 0.3, 0.5, 0.55, 0.6, 0.65$ ) and the kesterite-type ( $x = 0.7, 0.8, 0.9, 1.0$ ) structures linearly evolve with increasing zinc content  $x$ . Smaller zinc contents result in smaller  $c/a$  ratios and greater lattice distortion, leading to lower thermal conductivity. The Seebeck coefficient tends to decrease with increasing Zn content, whereas the electrical and thermal conductivities tend to increase. A maximum  $ZT$  of 0.23 was obtained for the sample of  $\text{Cu}_2\text{Cd}_{0.4}\text{Zn}_{0.6}\text{SnSe}_4$  at 720 K.

#### Acknowledgments

This work was supported by the National Natural Science Foundation of China (Nos. 51101103 and 51171117) and Shenzhen Science and Technology Research Grants (Nos. JC201005280515A, JCYJ20120613115247045, and JCYJ20130329104944 356).

#### References

- [1] Goldsmid HJ. Introduction to thermoelectricity. In: Hull R, Osgood Jr RM, Parisi J, Warlimont H, editors. Springer series in materials science, vol. 121. Springer; 2010. p. 242.
- [2] Snyder GJ. General principles and basic considerations. In: Rowe DM, editor. Thermoelectric Handbook CRC Press; 2006. pp. 28–41.
- [3] Snyder GJ. Thermoelectric power generation: efficiency and compatibility. In: Rowe DM, editor. Thermoelectrics Handbook CRC Press; 2006. p. 143.
- [4] Koumoto K, Mori T. Thermoelectric nanomaterials. In: Springer series in materials science, vol. 182. Heidelberg: Springer; 2013. pp. 1–375.
- [5] MacDonald DKC. Thermoelectricity: an introduction to the principles. New York, London: John Wiley & Sons, Inc.; 1962. p. 133.
- [6] Biswas K, He JQ, Blum ID, Wu CH, Hogan TP, Seidman DN, et al. High-performance bulk thermoelectrics with all-scale hierarchical architectures. *Nature* 2012;489:414–8.
- [7] Hsu KF, Loo S, Guo F, Chen W, Dyck JS, Uher C, et al. Cubic  $\text{AgPb}_m\text{SbTe}_{2+m}$ : bulk thermoelectric materials with high figure of merit. *Science* 2004;303:4.
- [8] Tsujii N, Mori T. High thermoelectric power factor in a carrier-doped magnetic semiconductor  $\text{CuFeS}_2$ . *Appl Phys Exp* 2013;6:043001.
- [9] Lu X, Morelli DT. Rapid synthesis of high-performance thermoelectric materials directly from natural mineral tetrahedrite. *MRS Commun* 2013;3: 129–33.
- [10] Liu HL, Shi X, Xu FF, Zhang LL, Zhang WQ, Chen LD, et al. Copper ion liquid-like thermoelectrics. *Nat Mater* 2012;11:422–5.
- [11] Matsushita H, Maeda T, Katsui A, Takizawa T. Thermal analysis and synthesis from the melts of Cu-based quaternary compounds Cu–III–IV–VI<sub>4</sub> and Cu<sub>2</sub>–II–IV–VI<sub>4</sub> (II = Zn, Cd; III = Ga, In; IV = Ge, Sn; VI = Se). *J Cryst Growth* 2000;208:416–22.
- [12] Liu ML, Chen IW, Huang FQ, Chen LD. Improved thermoelectric properties of Cu-doped quaternary chalcogenides of  $\text{Cu}_2\text{CdSnSe}_4$ . *Adv Mater* 2009;21: 3808–12.
- [13] Shi XY, Huang FQ, Liu ML, Chen LD. Thermoelectric properties of tetrahedrally bonded wide-gap stannite compounds  $\text{Cu}_2\text{ZnSn}_{1-x}\text{In}_x\text{Se}_4$ . *Appl Phys Lett* 2009;94:122103.
- [14] Raju Ch, Falmbigl M, Rogl P, Yan X, Bauer E. Thermoelectric properties of chalcogenide based  $\text{Cu}_{2+x}\text{ZnSn}_{1-x}\text{Se}_4$ . *AIP Adv* 2013;3:032106.
- [15] Fan FJ, Yu B, Wang YX, Zhu YL, Liu XJ, Yu SH, et al. Colloidal synthesis of  $\text{Cu}_2\text{CdSnSe}_4$  nanocrystals and hot-pressing to enhance the thermoelectric figure-of-merit. *J Am Chem Soc* 2011;133:15910–3.
- [16] Nakamura S, Maeda T, Wada T. Phase stability and electronic structure of in-free photovoltaic materials  $\text{Cu}_2\text{IIISnSe}_4$  (II: Zn, Cd, Hg). *Jpn J Appl Phys* 2011;50:05FF01.
- [17] Gao F, Yamazoe S, Maeda T, Wada T. Structural study of Cu-deficient  $\text{Cu}_{2(1-x)}\text{ZnSnSe}_4$  solar cell materials by X-ray diffraction and X-ray absorption fine structure. *Jpn J Appl Phys* 2012;51:10NC28.
- [18] Sachanyuk VP, Oleksyuk ID, Parasyuk OV. X-ray powder diffraction study of the  $\text{Cu}_2\text{Cd}_{1-x}\text{Mn}_x\text{SnSe}_4$  alloys. *Phys Status Solidi A* 2006;203:459–65.
- [19] Glen AS. New materials and performance limits for thermoelectric cooling. In: Rowe DM, editor. Thermoelectrics handbook. USA: CRC Press; 1995. p. 409.
- [20] Matsushita H, Ichikawa T, Katsui A. Structural, thermodynamical and optical properties of  $\text{Cu}_2\text{II-IV-VI}_4$  quaternary compounds. *J Mater Sci* 2005;40: 2003–5.
- [21] B. AXS, TOPAS V2.1: general profile and structure analysis software for powder diffraction data. User's manual. Karlsruhe, Germany: Bruker AXS; 2003.
- [22] Shannon R. Revised effective ionic radii and systematic studies of interatomic distances in halides and chalcogenides. *Acta Crystallogr A* 1976;32: 751–67.
- [23] Schorr S. The crystal structure of kesterite type compounds: a neutron and X-ray diffraction study. *Sol Energy Mater Sol Cells* 2011;95:1482–8.
- [24] Chen SY, Walsh A, Gong XG, Wei SH. Classification of lattice defects in the kesterite  $\text{Cu}_2\text{ZnSnS}_4$  and  $\text{Cu}_2\text{ZnSnSe}_4$  earth-abundant solar cell absorbers. *Adv Mater* 2013;25:1522–39.
- [25] Keyes WR. High-temperature thermal conductivity of insulating crystals: relationship to the melting point. *Phys Rev* 1959;115:564–7.